In situ X-ray diffraction of prototype sodium metal halide cells: Time and space electrochemical profiling

Job Rijssenbeek [a,*], Yan Gao [a], Zhong Zhong [b], Mark Croft [c,b], Najeh Jisrawi [d], Alexander Ignatov [e], Thomas Tsakalakos [e]

[a] GE Global Research, One Research Circle, CEB 109, Niskayuna, NY 12309, United States
[b] National Synchrotron Light Source, Brookhaven National Laboratory, Upton, NY 11973, United States
[c] Department of Physics and Astronomy, Rutgers University, 136 Frelinghuysen Road, Piscataway, NJ 08854, United States
[d] Department of Applied Physics, University of Sharjah, POB 27272, Sharjah, United Arab Emirates
[e] Materials Science and Engineering Department, Rutgers University, Piscataway, NJ 08854, United States

ABSTRACT

The feasibility of using energy dispersive X-ray diffraction to characterize full size battery cells is demonstrated by unprecedented in situ measurements of the electrochemical processes taking place inside high temperature sodium metal halide (Na/MCl$_2$, M = Ni and/or Fe) cells during charge/discharge cycling. Diffraction data provide phase information either via line scans across the 5 cm wide cells or via fixed location scans as a function of time. The data confirm the propagation of a well-defined chemical reaction front, as a function of charge/discharge time, beginning at the ceramic separator and proceeding inward. Measurement of the temporal evolution of the phase abundances yields mechanistic understanding and reaction rates as a function of charge/discharge state. In the case where M includes Fe, the data also clearly show the appearance of an intermediate phase, Na$_6$FeCl$_8$, during charging, thereby underscoring the power of this technique to reveal subtle mechanistic information. A number of additional detailed electrochemical kinetic effects are also discussed. This study shows that in situ high energy X-ray diffraction characterization of advanced battery cells in space and time is eminently feasible on a routine basis, and has great potential to advance the understanding of "buried" chemical processes.

© 2010 Elsevier B.V. All rights reserved.

1. Introduction

As advanced battery technologies progress towards large-scale application, an in-depth fundamental understanding of their complex chemical processes, degradation pathways, and failure modes in full-size cells is required. Despite tremendous technical progress over decades of research and development in battery technologies, too little is known about the evolution of microstructure (especially in the cathodes), mechanisms of charge transport, nature of the phase changes that take place during electrochemical cycling, and details of degradation and failure modes. These limitations are frequently the result of the traditional inaccessibility during cycling of the batteries' active components. Elucidating and quantifying the chemical processes that occur in full-size cells under operating conditions is key to enhanced power and energy densities, longer life, and greater safety. in situ characterization of the cathode, separator, electrolyte, and anode materials as a function of time, state of charge, stress, temperature, etc. would be a breakthrough for battery development.

The advent of electrochemical cells with X-ray transparent windows has made in situ synchrotron X-ray techniques an important battery characterization tool, especially for lithium-based batteries [1–3]. Such X-ray studies, typically employing energies of 7–20 keV, provide mechanistic insight, validation of theoretical modeling and a check on empirical chemical modifications designed to optimize advanced batteries. However, to assure X-ray transparency, these in situ experiments have relied on thin pouch cells or windowed cells specifically designed for in situ work [4]. Such geometries are convenient for fundamental studies but are often far removed from the commercial cell geometries, and window materials often limit the cycling conditions that can be investigated. This is especially true for sodium metal halide cells, which operate at 300 °C and are over 3 cm thick (see Fig. 1) [5–7].

The central purpose of this paper is to demonstrate the potential of the in situ energy dispersive X-ray diffraction (EDXRD) technique to further understanding of traditionally inaccessible batteries during operation. The vehicles for this demonstration are full-size prototype sodium metal halide cells. EDXRD exploits deeply penetrating high-energy radiation for high resolution phase and strain mapping deep in the interior of bulk engineering materials [8–13]. By applying EDXRD to battery research, the benefits of in situ X-ray diffraction can be extended from electrochemical cells
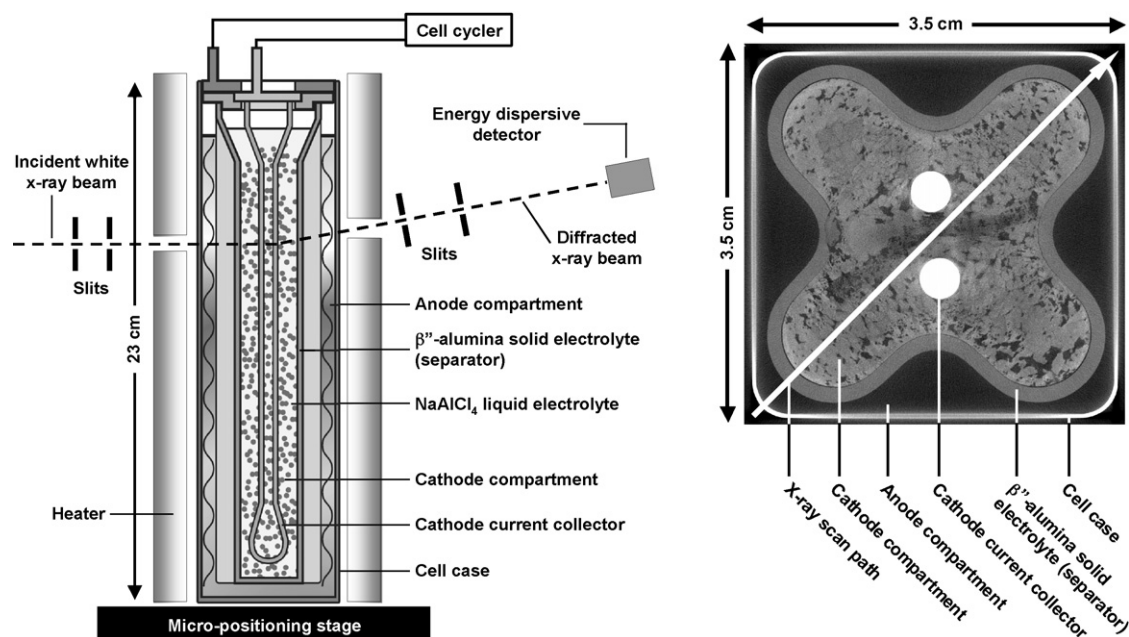
Fig. 1. (a) Schematic of a sodium metal halide cell in the in situ synchrotron EDXRD experimental setup. (b) Cross-sectional computed tomography image of a cell. The arrow along the cell diagonal denotes the path of the X-ray line scans used in this work. This corresponds to an X-ray penetration depth of up to 50 mm.

designed specifically for X-ray transparency, to the full panoply of prototype and production cells. The ability to spatially and temporally characterize the cell charge-state variations as a function of cycling conditions, via the local crystal structure or phase distribution, should enable direct feedback into the battery design optimization process. Furthermore, diffraction-determined charge state distribution and evolution profiles will help validate and augment theoretical models.

Sodium-metal-halide technology excels in applications requiring high energy density. In the last few years, General Electric has refined the sodium-metal-halide technology such that it is now sufficiently developed for application in heavy-duty transportation and stationary power quality applications. The new technology (NaMx) is superior to the incumbent lead acid batteries in performance, and is expected to have the lowest life cycle cost of any battery technology for these applications. In the near future, high energy density batteries will be required to achieve commercially viable (hybrid) electric vehicles that can travel long distances on battery power alone. Large-scale penetration (greater than ~20%) of intermittent renewable energy sources (e.g., wind and solar) will also require high energy density electricity storage to mitigate the grid instability they introduce. These growing markets are driving a renewed interest in the sodium metal halide technology.

The sodium metal halide cell consists of a solid metal and sodium chloride positive electrode that is separated from a liquid sodium negative electrode by a ceramic β''-alumina solid electrolyte (BASE) tube (Fig. 1) [5–7]. It operates at 300 °C, a temperature at which the sodium and catholyte (NaAlCl$_4$) are molten, and the ionic conductivity of the BASE is high. On charge, the metal, iron and/or nickel in this study, in the positive electrode (cathode) is oxidized (reaction (1)) and combines with chloride ions dissolved in the liquid electrolyte to form a metal dichloride (reaction (2)). The electrons extracted in reaction (1) travel through the external circuit. Meanwhile, sodium chloride dissolves in the electrolyte to replenish the chloride ions (reaction (3)). The sodium ion diffuses via the liquid electrolyte and then through the ceramic electrolyte. It is reduced to metallic sodium by electrons from the circuit upon entering the negative electrode (anode) compartment (reaction (4)). The net charging reaction forms sodium metal in the anode and metal chlo-

ride in the cathode (reaction (5)). Only approximately one-third of the metal is converted to metal chloride leaving a continuous electrically-conductive current collecting network. On discharge, the process is reversed.

$$M \rightarrow M^{2+} + 2e^- \tag{1}$$

$$M^{2+} + 2Cl^- \rightarrow MCl_2 \tag{2}$$

$$NaCl \rightarrow Na^+ + Cl^- \tag{3}$$

$$Na^+ + e^- \rightarrow Na \tag{4}$$

$$Net : 2NaCl + M \rightarrow 2Na + MCl_2 (M = Ni\,and/or\,Fe) \tag{5}$$
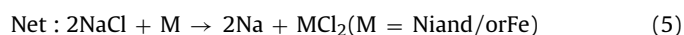
The open circuit voltage (OCV) of such cells is 2.58 V for M = Ni and 2.35 V for M = Fe.

Among the attractive features of the NaMx technology are: high energy density (120 Wh kg^{-1}; 320 Wh L^{-1} at the battery pack level); long lifetimes under repeated cycling; insensitivity to extreme temperature environments; overcharge and overdischarge tolerance; battery resilience to multiple cell failures; and good safety performance under catastrophic mechanical impact [6]. The large cell size and complex electrochemistry of this battery technology provide an excellent proving ground to establish both the penetrating power and detailed structural insights possible with EDXRD.

2. Experimental

2.1. NaMx electrochemical cell

Fig. 1 shows (a) a side-view cell-schematic and (b) X-ray computed tomography (CT) cross-sectional view of a typical NaMx cell studied in this work. The cell is 23 cm in height and has a 3.5×3.5 cm^2 square cross-section. To maintain the 300 °C operating temperature, the cell was positioned inside a rectangular aluminum sleeve with attached heating elements, and was wrapped in thermal insulation. The cell and heater assembly were mounted on a computer-controlled x–y–z platform with a positioning accuracy of about 1 μm. The incident and diffracted X-ray beam paths are indicated in Fig. 1(a). The spatial profiling is achieved by

monitoring the diffraction signal from a fixed region in space while using the x–y–z platform to position various portions of the cell into the probed region (see the discussion below).

2.2. Energy dispersive X-ray diffraction

The energy dispersive X-ray diffraction (EDXRD) measurements used for this work were performed at the Brookhaven National Synchrotron Light Source (NSLS) on the superconducting wiggler beam line X17B1. In general, EDXRD has proven highly effective for strain and phase mapping in engineering applications [8–13]. The experimental setup [8–12] involves "white beam" incident radiation with scattering at a fixed angle 2θ ($2\theta = 4°$ in the present work). The transmission diffraction geometry and incident/scattered beam collimation slits are shown schematically in Fig. 1(a). A high resolution Germanium detector measures the intensity versus energy of the scattered beam. The energies, E, of the scattered Bragg peaks are given by $E = b/[d_{hkl} \sin(\theta)]$ where d_{hkl} is the spacing associated with a specific inter-atomic plane labeled by the Miller indices (hkl). Here $b = hc/2$ where h is Plank's constant, and c is the speed of light. In the conventional units where d_{hkl} is measured in Angstroms and E in keV one has $b = 6.199$ Å keV.

In strain profiling applications, variations of the inter-atomic spacings with position are used to determine the strain variations. Because the central focus of this work is on phase mapping, we use a set of characteristic Bragg reflections as the diffraction "fingerprint" for identifying a given crystalline chemical phase. The relative intensity variations, in time or space, of these reflections serve as a proxy for the relative abundance of the respective phases. Quantitative determination of phase abundances is complicated by the variable scattering factor as a function of diffracted energy, and strong variations in the absorption effects with energy and depth-in-cell. Although tractable, as indicated by the recent work of Scarlett et al. [14], these issues are beyond the scope of the present work. For our purposes, simple comparison of the intensities of characteristic Bragg lines yields a satisfactory picture of the relative phase variations.

The intersection of the incident and diffracted beam paths defines the gauge volume (GV) over which the crystalline scattering is averaged [8,13]. In this work the GV dimensions were 0.1 mm in height (along the long cell dimension) and 1 mm in width (perpendicular to both the long-cell dimension and the beam direction, see Fig. 1(b)). Along the incident beam direction the small angle leads to spreading of the GV and to a length of 3 mm [13]. The EDXRD should be performed in the regime where the diffraction signal can be averaged over a large number of grains with random orientations. To help achieve this, a vertical oscillation of the GV position over a distance of 6 mm along the long-cell axis was executed while collecting a given spectrum.

For this work, it is highly advantageous to quickly compare intensities of multiple Bragg lines from multiple phases for many diffraction spectra taken as a function of position or cell state-of-charge (SoC). We developed an interactive data language (IDL) program which constructs 2D contour plots of diffracted X-ray intensity (in grayscale) versus the diffracted energy (E) on the abscissa and the spectrum number (N) on the ordinate to allow quick identification of the appearance or disappearance of crystalline phases. Spectra were collected at equal time or spatial position intervals, thus N is directly proportional to either time (in a fixed location measurement) or spatial position across the interior of the cell (in a line scan measurement).

A more quantitative estimate of the varying abundance of different crystalline phases can be obtained by integration of characteristic diffraction peak(s) using a user-define energy window. A Linux-based script was implemented to plot relative integrated peak intensity versus spectrum number during or immediately
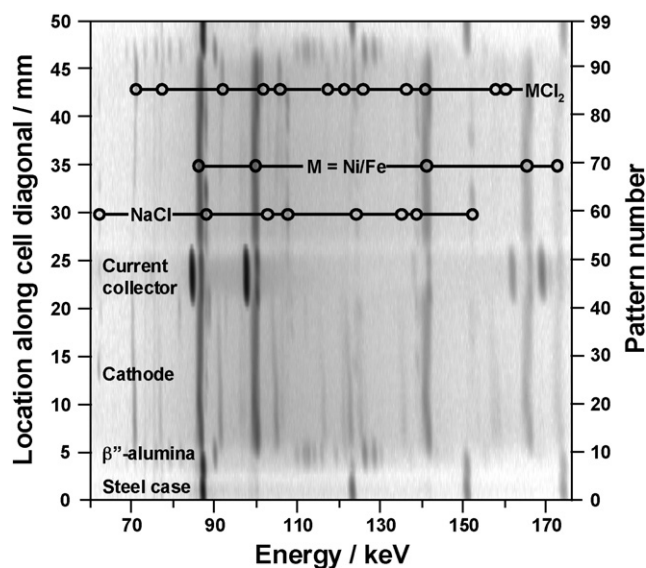
Fig. 2. Diffraction intensity contour plot of 99 diffraction patterns taken in 0.5 mm increments along the cell diagonal, as depicted in Fig. 1(b). The x-axis corresponds to the diffracted X-ray energy, and the y-axis is location along the cell diagonal.

after a data collection sequence. This windowed-integration technique is especially useful when multiple Bragg lines are closely spaced or partially overlapping, or where a suitable background for data fitting is difficult to establish quickly.

In cases where diffraction peaks are sufficiently isolated we can employ an automated batch mode Gaussian peak fitting routine (using a local spline fit background). This fitting technique was developed for strain field profiling and can also be applied during or immediately after a data collection sequence. The windowed-integration and Gaussian fitting estimates of Bragg line intensity variations compare very favorably, as will be shown below.

3. Results and discussion

3.1. Initial spatial phase distribution in cell

Fig. 2 shows a greyscale contour plot, of the type described above, for a sequence of diffraction spectra taken along a cell-diagonal path (as shown by the arrow in Fig. 1(b)). The characteristic Bragg lines of the various components of the cell are indicated in Fig. 2: as scanned, from the outside in, the steel casing; the β''-alumina separator; the cathode (M, MCl_2 and NaCl); and the central positive current collector.[1] The diffraction-defined regions can be mapped one-for-one to those in the CT image in Fig. 1(b). The distibution of phases is consistent with results from ex situ investigations.

3.2. Phase evolution during cell charging

To study the phase evolution during cell charging, the diffraction-gauge volume (GV) was positioned in the cathode just inside the β''-alumina separator. A sequence of 99 diffraction spectra, each collected for 70 s, were then taken as the cell was charged at 10 A constant current (approximately C/3 rate). Fig. 3(a) displays these diffraction spectra in the form of a contour plot of scattered intensity (grayscale), versus scattered X-ray energy, and file

---

[1] The JCPDS files used for peak indexing were: NaCl PDF #00-005-0628; $FeCl_2$ PDF #070-1634; $NiCl_2$ PDF #01-071-2032, JCPDS Na_6MnCl_8 PDF #01-070-0841 (the file for isostructural Na_6FeCl_8 does not exist); Ni PDF #00-004-0850.
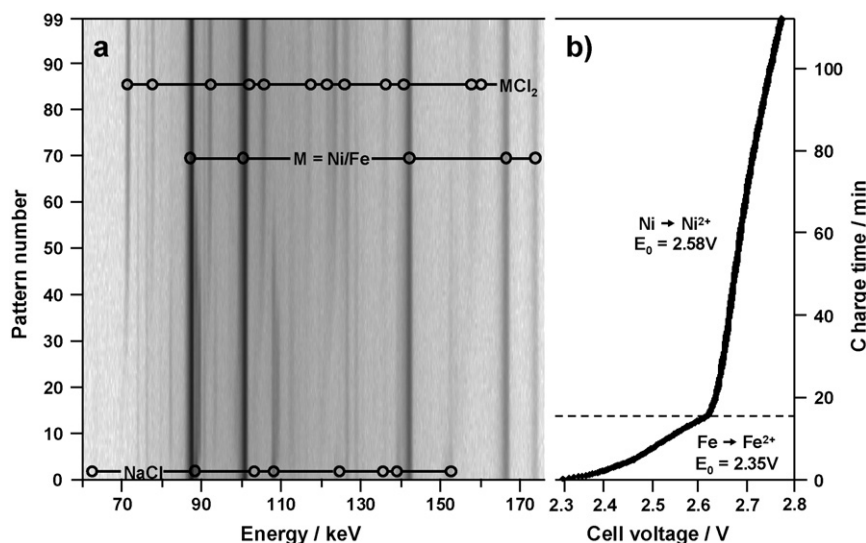
Fig. 3. (a) Diffraction intensity contour plot of a sequence of 99 in situ diffraction spectra taken with the beam positioned at a fixed location inside the cell during a 10 A charge. (b) The simultaneously collected voltage versus time cell charging curve. The dominant metal species being oxidized are shown.

number (or charge time) on the vertical axis. Fig. 3(b) shows the simultaneously collected cell voltage versus time data. The in situ data reaffirm the expected reaction pathway. Peaks for NaCl disappear with charge time to be replaced by MCl_2 peaks (note the transition between $N = 40$ and 60). Only approximately one-third of the metal is consumed by the reaction with NaCl therefore a change in the intensity of the M peaks is difficult to discern in this view. With some scrutiny, the presence of an intermediate phase is apparent from $N = 5$ to 40.

Fig. 4(a and b) shows diffraction spectra that illustrate the Bragg peaks of the various phases. In addition to the principal phases already discussed, diffraction peaks from an additional intermediate phase, Na_6MCl_8, are identified in Fig. 4 [15,16]. The strongest of these occur just to the high energy side of NaCl phase lines and can be seen by careful inspection of Fig. 3. To better visualize the characteristic peaks of the intermediate phase, Fig. 5 presents an narrower energy range view of the contour plot in Fig. 3(a).

Suzuki phases with composition Na_6MCl_8 are well-known in $NaCl:MCl_2$ systems where M is a divalent cation [17–19], and have previously been detected in Na/MCl_2 cells charged at low currents [15,16]. The Suzuki phase precipitates within the host NaCl lattice forming a superstructure with an 8-fold larger unit cell (i.e., twice that of NaCl along each axis) due to ordering of the divalent cation and the induced sodium vacancy. In this framework, the formula can be expressed as $\{Na_{3/4}[\square_{1/8}M_{1/8}]\}Cl$, where $\square$ represents a vacancy on the sodium site. While phases of this structure with M = Cr, V, Mn and Fe are known, the M = Ni phase has not been reported, nor has it been observed electrochemically in our cell tests, likely due to its small ionic radius relative to Na ($r_{Ni} = 0.69$ Å; $r_{Na} = 1.02$ Å). Furthermore, our ex situ elemental analysis of NaCl crystals by energy dispersive X-ray spectroscopy in scanning electron microscopy reveals the presence of Fe but never Ni. This evidence suggests that the Na_6MCl_8 phase, observed in this study contains essentially only M = Fe with modest if any Ni content.

3.3. NaCl, MCl_2, and Na_6MCl_8 phases

Fig. 6(a and b) shows the window-integrated intensities for selected NaCl, MCl_2, and Na_6MCl_8 diffraction peaks plotted versus pattern number (or charge time). The specific spectral windows are indicated by horizontal lines above the peaks of interest in Fig. 4(a). The MCl_2 peaks are all well isolated, allowing their

entire intensity (plus background) to be captured. The overlap of the NaCl (2 2 0)/Na_6MCl_8 (4 4 0) reflections, and the NaCl (2 2 2)/Na_6MCl_8 (4 4 4) reflections, necessitated choosing integration ranges that sampled only portions of the respective Bragg
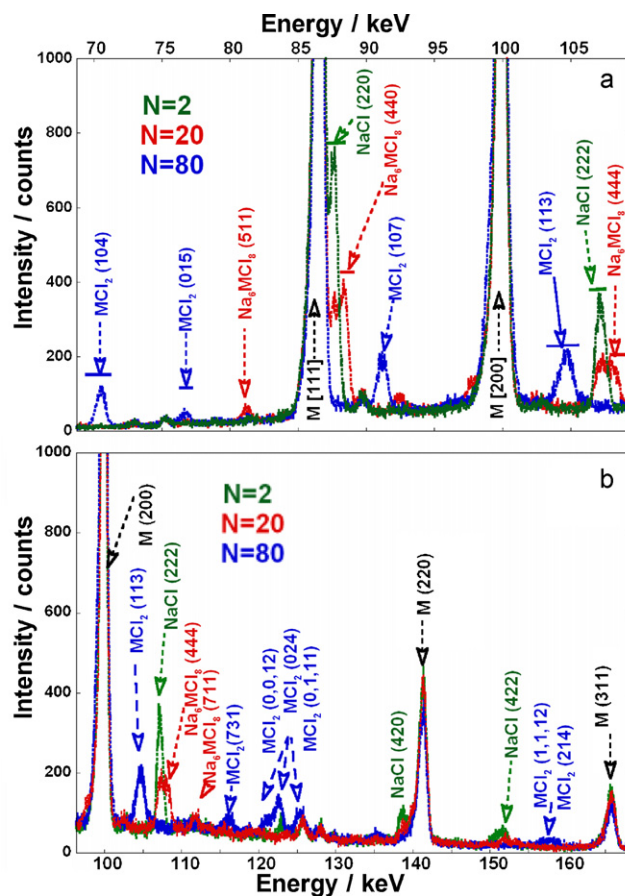
Fig. 4. (a) Selected 1D diffraction patterns showing the specific Bragg peak positions for M, NaCl, MCl_2, and Na_6FeCl_8 phases (M = Ni and Fe). The horizontal lines over individual peaks indicate the energy windows used for integration of representative peak intensity for a given phase. Because the major NaCl and Na_6FeCl_8 peaks cannot be unambiguously resolved, the integration region spans only the portion of the peak width for which the overlapping line intensity is deemed negligible.
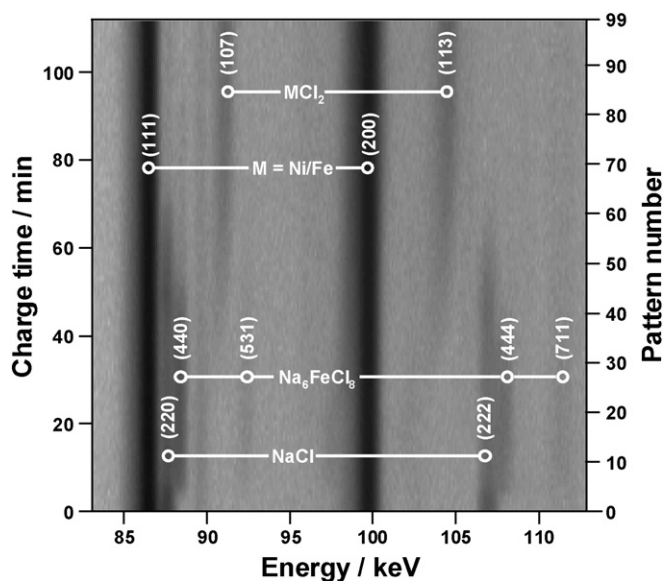
Fig. 5. Expanded view of the diffraction intensity contour plot shown in Fig. 3(a). The Miller indices of the Bragg reflections of the M, NaCl, MCl_2, and Na_6FeCl_8 (M = Ni and Fe) phases are indicated. Note the transformation, bottom to top, of the NaCl, first to Na_6FeCl_8 and then to MCl_2.

peaks. Here the integration ranges were chosen to qualitatively maximize the phase-related-intensity and minimize the nearby line contribution. Furthermore, the proximity of the NaCl (2 2 0) and Na_6MCl_8 (4 4 0) lines to the strong Ni (1 1 1) line necessitated additional care in choosing these integration windows. Using these partial-area results from overlapping lines necessitates the assumption of constant peak shape and centrum. Such compromises notwithstanding, this method appears highly useful for estimating the relative time/charging induced changes in phase content.

Fig. 6(c) shows the derivatives, dI/dN, of the window-integrated spectral intensities plotted in Fig. 6(b). Fourier smoothing of the original data was used to reduce the scatter in the numerical differentiation process. The data illustrate the basic charging phenomena transpiring in the cell; namely the transformation of sodium chloride based phases (NaCl and Na_6MCl_8) to metal chloride (and liquid sodium in the anode, which is not captured here). This transformation is manifested in Fig. 6(a and b) by the appearance and subsequent increase in intensity of the MCl_2 (1 1 3) diffraction peak starting after N = 25 concomitant with the steady disappearance of the NaCl-based phases. The appearance and disappearance of the intermediate Na_6MCl_8 phase highlight the complexity of the electrochemistry involved.

To facilitate discussion of the phase transformations, the charge process can be broken into four segments of interest, as indicated in Fig. 6. Initially, NaCl is the sole chloride phase, consistent with a fully discharged cell. Segment 1 is marked by the growth of the Na_6MCl_8 phase and loss of the NaCl phase, which reach maximal rates of change at N ∼ 5. During this time, the cell voltage rises rapidly from 2.3 V, indicative of iron oxidation, to 2.64 V, indicative of Ni oxidation (Fig. 3). The conversion of NaCl to Na_6MCl_8 in this region is abundantly clear from the rapid and simultaneous changes with opposite signs in the characteristic peak intensities of these two phases. That no $FeCl_2$ is observed during this time suggests that initially all the iron that is oxidized becomes incorporated into the NaCl as Na_6FeCl_8. Therefore $FeCl_2$, generated at the M electrode, must be transported (likely as $FeCl_4^{2-}$) to the NaCl where it precipitates as the Suzuki phase on the surface. The incomplete conversion of the NaCl to Na_6FeCl_8 is unexpected, as there is enough Fe in the cell to convert all the NaCl into Na_6FeCl_8, but could
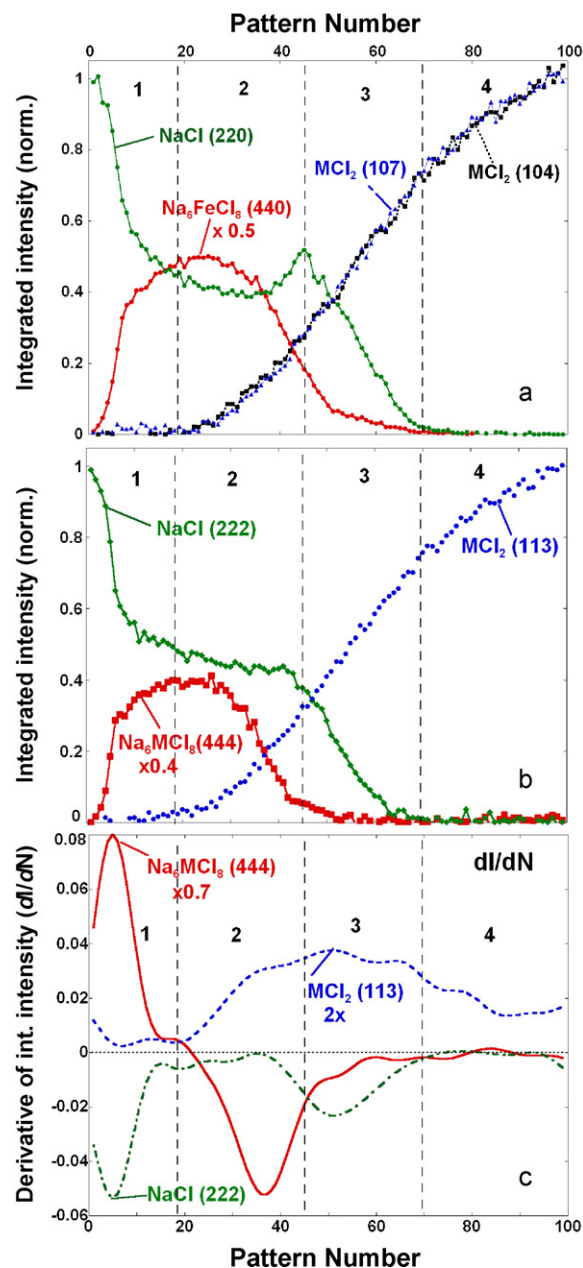
Fig. 6. (a) and (b) Variation of integrated spectral intensities versus pattern number (charge time) for Bragg reflections chosen as proxies for the relative phase abundances of NaCl, MCl_2, and Na_6MCl_8. The integrated areas have been normalized to the maximum value for a given phase; the Na_6MCl_8 curves are reduced in magnitude as indicated for clarity. (c) Derivative curves, dI/dN, of the intensity curves in b. The intensity curves were Fourier smoothed before the numerical derivative was taken. The MCl_2, and Na_6MCl_8 derivative curves have been scaled as indicated for clarity. The charge process has been divided into four segments for the purposes of discussion in the text and are numbered accordingly in each figure.

be the result of the Na_6FeCl_8 forming a passivating layer on the NaCl.

In segment 2, peaks for MCl_2 emerge and the Na_6MCl_8 phase is consumed. The slower increase in voltage in this region (Fig. 3) indicates that Ni oxidation is the now the dominant cell reaction. Formation of MCl_2 is evidenced by increased intensity of its characteristic peaks. The growing MCl_2 peaks undergo a subtle shift to higher energy. This is consistent with increasing Ni content in the MCl_2 phase and is discussed in more detail below. The downturn in the Na_6MCl_8 intensity curves and stable (or even increasing) NaCl curves indicate that MCl_2 is generated predominantly at the
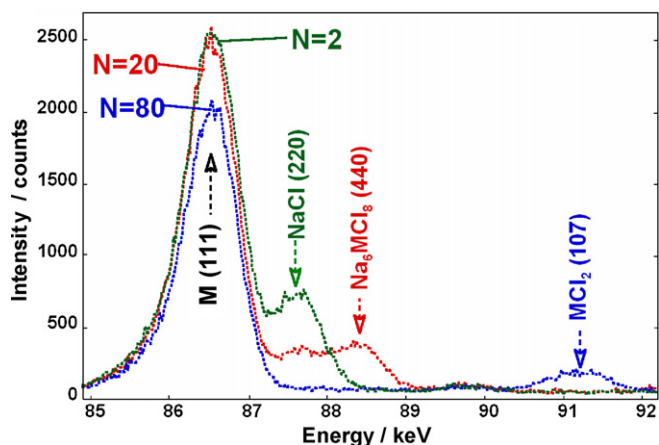
Fig. 7. Expanded view of the region around the M (1 1 1) peak from three scans during charging. The intensity decrease with time is the result of conversion of M to MCl_2.

Fig. 8. The window-integrated intensity versus diffraction pattern number for the (1 1 1) (solid red line), (2 2 0) (green dash-dot line) and (3 1 1) (black circles), reflections of the metal (left axis); and the MCl_2 (1 0 7) reflection (blue dashes; right axis). Integrated intensities are corrected for background intensity and are normalized to their maximum values. (For interpretation of the references to colour in this figure legend, the reader is referred to the web version of the article.)

expense of the Suzuki phase, not NaCl. This supports the idea that the Suzuki phase forms as a layer on the NaCl. Curiously, the NaCl (2 2 0) peak suggests that NaCl momentarily increases in abundance at the end of the segment, although an increase is not observed in the NaCl (2 2 2) peak. Any proposed mechanism that explains this short-lived increase in NaCl (2 2 0) would be speculative at this point but the electrochemical details revealed by our EDXRD technique are robust enough to introduce consideration and more detailed subsequent testing of such hypotheses.

Segment 3 is characterized by NaCl loss. The downturn in the NaCl intensity curves in Fig. 6(a and b) is clear and the negative peak in the NaCl (2 2 2) derivative curve in Fig. 6(c) coincides with the broad positive peak in the MCl_2 (1 1 3) derivative curve. Thus segment 3 constitutes the maximum of the NaCl to MCl_2 conversion reaction (with the concomitant generation of liquid sodium in the anode).

In segment 4, the NaCl peaks have disappeared yet the MCl_2 peaks continue to increase. This apparent contradiction suggests three possible explanations. The first is that significant NaCl is still available as nano-sized particles that do not diffract X-rays. The second is that the $NiCl_2$ precipitates as a poorly crystalline phase that continues to crystallize with time. Third, dissolved NaCl transported from other parts of the cell may continue to supply the reaction. The last explanation seems the most likely. Extensive SEM imaging has not revealed significant nano-NaCl or non-crystalline MCl_2, however, conclusive evidence remains elusive.

3.4. Conversion of M to MCl_2

The large excess of Ni/Fe makes fractional changes in M peak intensity difficult to discern in Figs. 3–5. Fig. 7 displays the regions around M (1 1 1) peak on a scale appropriate for illustrating its intensity variation. It manifests a relatively constant intensity between spectra 2 and 20 but decreases in intensity by $N = 80$. The M (2 2 0) and (3 1 1) lines show identical behavior as shown by their window-integrated intensities versus pattern number in Fig. 8. The MCl_2 (1 0 7) peak is both rather intense and well separated from other phase lines (Fig. 7), and its intensity is also plotted for reference (Fig. 8). Here the intensities have had their backgrounds subtracted and have been normalized to their maximal values to facilitate their comparison. With these normalizations the intensity curves in Fig. 8 provide estimates of fractional phase abundances.

The M-phase lines vary between 0.8 and 1.0. This is consistent with the participation of ~20% of the Fe–Ni in the cell reaction, leav-

ing about 80% to provide a network for electronic conduction. An inverse correlation between M and MCl_2 abundances is clear from the data in Fig. 8. Both curves exhibit a slope change near pattern number 20 and reach their midpoint near pattern number 55.

3.5. Peak fitting compared to windowed-integration analysis

As mentioned above, the MCl_2 peaks in the contour plots of Figs. 3 and 5 show a subtle yet systematic shift from lower energy to higher energy (i.e., contracting lattice parameters) right after its initial appearance. An expanded contour plot of the the MCl_2 (1 0 4) reflection is shown in Fig. 9(a). The shift is highlighted by the vertical dashed line in the figure. This behavior is also apparent in Fig. 9(b), which shows a series of MCl_2 (1 0 4) peaks at several points during charge. Because this peak is not overlapped by other peaks, we could apply a batch fitting method, developed by our group for strain profiling, to analyze this line. The fitting uses a local spline background and Gaussian peak shape. The fitted peak spectral area is plotted versus the spectrum number (charge time) in Fig. 10(a) together with the window-integrated area of the same line. The results demonstrate that there is good agreement between the two methods.
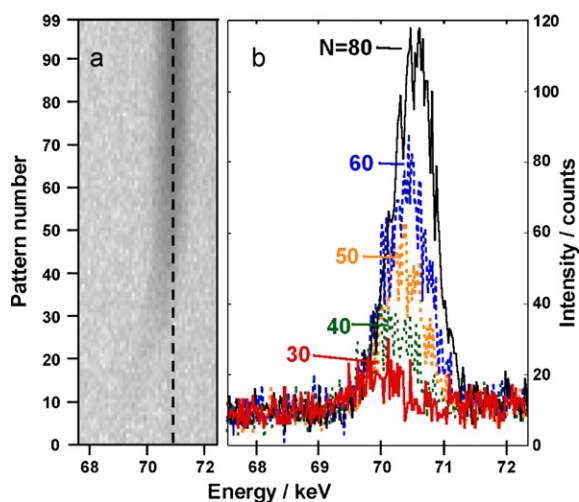
Fig. 9. (a) A section of the diffraction intensity contour plot shown in Fig. 3(a) around the MCl_2 (1 0 4) reflection. (b) Selected 1D diffraction patterns over the same energy range. Note the increase in intensity, and movement to higher energy, with increasing pattern number (charge time).
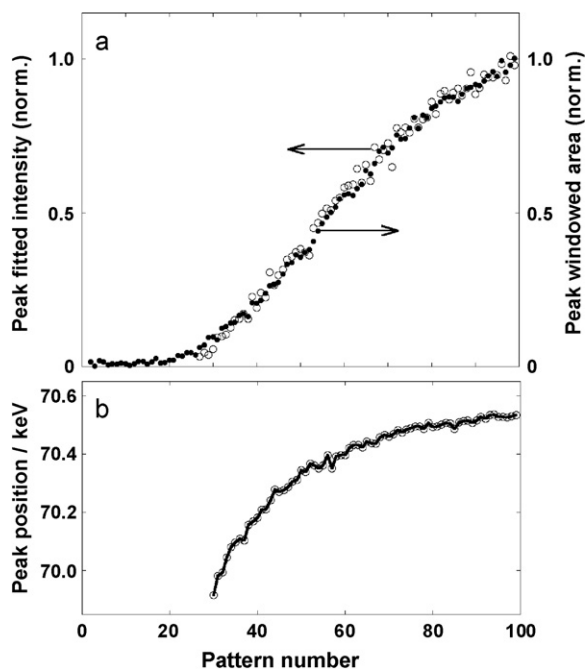
Fig. 10. (a) Comparison of the fitted-line intensity (open circles) to the window-integrated intensity (solid circles) for the MCl_2 (1 0 4) peak. The intensities have had their background subtracted and are normalized to their maximum value. (b) Position of fitted MCl_2 (1 0 4) Bragg peak versus pattern number (charge time).

The systematic shift of the MCl_2 (1 0 4) peak position to higher energies (noted qualitatively above) is quantitatively very clear from Fig. 10(b) and indicates a lattice parameter contraction with increasing state of charge. As noted above, the Fe to $FeCl_2$ reaction takes places at a lower cell voltage (2.35 V) than the Ni to $NiCl_2$ reaction (2.58 V) therefore the oxidation of Fe is expected to occur first and/or faster than that of Ni. Literature room temperature d_{104} values for $FeCl_2$ and $NiCl_2$ are respectively 2.5398 Å and 2.4787 Å (JCPDF #070-1634 and 01-071-2032, respectively) giving a change of $\Delta d_{104} = 0.061$ Å. Thus the observed effect ($\Delta d_{104} = 0.022$ Å) is qualitatively consistent with the evolution of a $Fe_{1-y}Ni_yCl_2$ phase in which the Ni content (y) increases with charge time. Thus these data show that charging the Ni/Fe system yields a single chloride phase, not two separate MCl_2 phases as might have been expected. Ex situ elemental analysis of metal halide crystals by energy dispersive spectroscopy during scanning electron microscopy analysis confirms the formation of a mixed-metal chloride phase.

3.6. Reaction front in space and its space–time evolution

The results above dealt with a high resolution characterization of the passage of a reaction front through a fixed point in the cell as a function of charging time. In this section, the characterization of reaction fronts in space will be considered at fixed charging times. The spatial progression of the reaction fronts through the cell with increasing charge times will also be shown.

Fig. 11 shows the spatial distribution of the phases as a function of position along the cell-diagonal at mid-cell height. This particular cell was discharged 50% at 32A (1C rate) from the fully charged state. The NaCl peaks (discharged state) can be seen near the BASE while the MCl_2 peaks (charged state) remains closer to the central current collector. Fig. 11(b) shows the window integrated Bragg intensities for the NaCl (2 2 0) and MCl_2 (1 0 7) reflections. The reaction front has moved inward uniformly away from the
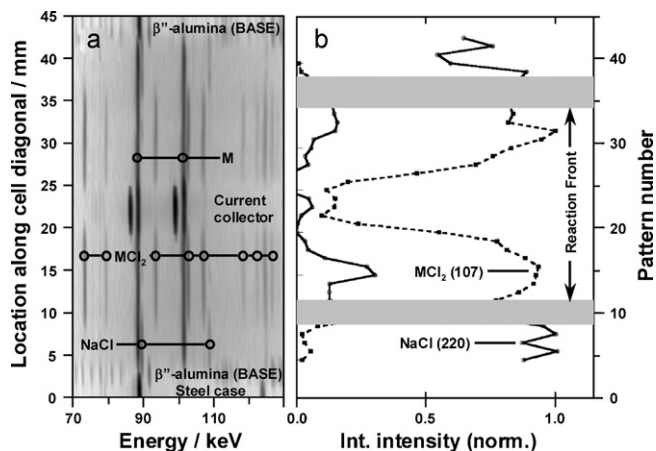
Fig. 11. (a) Intensity contour plot of 45 successive in situ diffraction patterns, taken along the diagonal of a half-discharged cell. (b) Matching window integrated intensities for the NaCl (2 2 0) and MCl_2 (1 0 7) Bragg reflections plotted versus location along cell diagonal. All integrated intensities have had their background subtracted and are normalized to their maximum value. Note the spatially resolved reaction fronts approximately 10 mm in from the β''-alumina separator (see approximately patterns 10 and 35).

BASE and is intersected by the line scan near patterns $N = 10$ and $N = 35$.

Fig. 12 provides temporal snapshots of the reaction front in a series of successive charging levels. The fully discharged contour plot (top) manifests only the NaCl phase as evidenced by its continuous lines across the entire cell diagonal. At 29% charged, the NaCl lines have receded, while the MCl_2 lines have begun growing inward from the BASE. In the 82% charged state, the NaCl phase has been consumed to near the central current collector and has
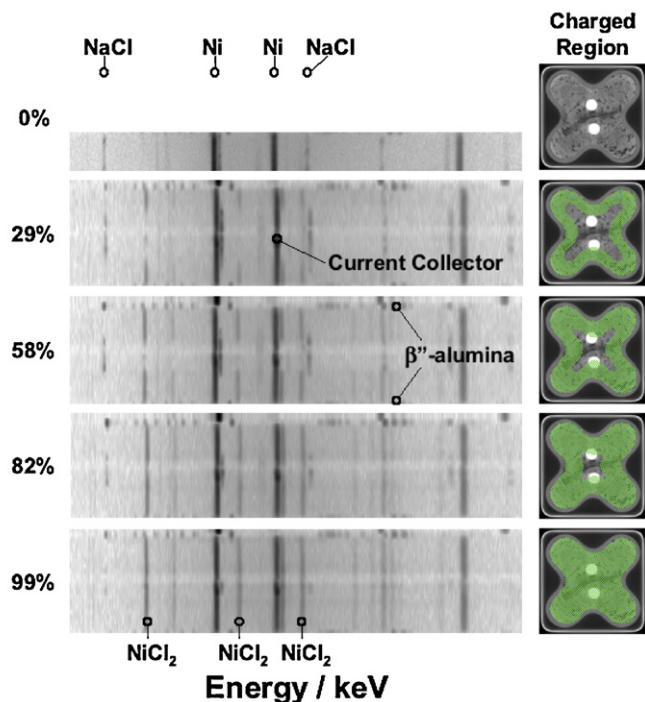
Fig. 12. Sequence of intensity contour plots depicting diffraction profiles across the center diagonal of a cell at varying states of charge from 0% (fully discharged; NaCl) to 99% (nearly fully charged; MCl_2 with only trace NaCl at center of cell). The spatial extent of NaCl and MCl_2 phases is indicated by their characteristic diffraction peaks as indicated. Note that the charging reaction progresses from the β''-alumina interface towards the center of the cell, which is shown schematically at right.

been replaced by the MCl_2 phase extending still deeper into the cell. Finally, in the 99% charged scan, only a vestigial trace of the NaCl phase remains near the cell center and the MCl_2 phase lines extend across the entire cell diagonal.

4. Conclusions

In this paper the detailed electrochemical phase transformations in a prototype $NaCl/MCl_2$ cell have been profiled, using EDXRD, as a function of state of charge and as a function of position in the interior of the cell. We have tracked the coming and going of each major phase in the cell directly throughout a full charge. The diffraction evidence of the NaCl, M, MCl_2 and Na_6FeCl_8 phases has demonstrated the complexity underlying the charging reaction (5). The clear observation of Na_6FeCl_8 preceding the NaCl to MCl_2 transformation provides a dramatic illustration of the electrochemical detail achievable through the EDXRD method. The charge time profiling at a fixed position in a cell was sufficiently detailed that the derivative (with respect to time) of the relative phase abundances could be calculated and the relative kinetic transformation rates discussed. Spatial phase profiling, at fixed charge time, has visualized the well-defined reaction front in these cells. Moreover, similar profiles at different charge times have shown the progression of the front from the outside of the cathode toward the center. These results corroborate previous findings and have demonstrated that in situ high energy X-ray diffraction characterization, in space and time, of advanced battery cells under realistic cycling conditions are eminently feasible on a routine basis. The technique will aid the advancement of battery technology by enabling the study of the fundamental mechanisms at work inside commercially relevant cells of any battery type.

Acknowledgements

References

[1] J.R. Dahn, R.R. Haering, Solid State Commun. 40 (1981) 245.
[2] J.-M. Tarascon, A.S. Gozdz, C. Schmutz, F. Shokoohi, P.C. Warren, Solid State Ionics 86–88 (1996) 49.
[3] S. Mukerjee, T.R. Thurston, N.M. Jisrawi, X.Q. Yang, J. McBreen, M.L. Daroux, X.K. Xing, J. Electrochem. Soc. 145 (1998) 466.
[4] M. Morcrette, Y. Chabre, G. Vaughan, G. Amatucci, J.-B. Leriche, S. Patoux, C. Masquelier, J.-M. Tarascon, Electrochim. Acta 47 (2002) 3137.
[5] J.L. Sudwoth, J. Power Sources 100 (2001) 149.
[6] C.-H. Dustman, J. Power Sources 127 (2004) 85.
[7] X. Lu, G. Xia, J.P. Lemmon, Z. Yang, J. Power Sources 195 (2010) 2431.
[8] M. Croft, I. Zakharchenko, Z. Zhong, Y. Gulak, J. Hastings, J. Hu, R. Holtz, M. DaSilva, T. Tsakalakos, J. Appl. Phys. 92 (2002) 578.
[9] M. Croft, Z. Zhong, N. Jisrawi, I. Zakharchenko, R.L. Holtz, Y. Gulak, J. Skaritka, T. Fast, K. Sadananda, M. Lakshmipathy, T. Tsakalakos, Int. J. Fatigue 27 (2005) 1409.
[10] M. Croft, N. Jisrawi, Z. Zhong, R. Holtz, K. Sadananda, J. Skaritka, T. Tsakalakos, Int. J. Fatigue 29 (2007) 1726.
[11] M. Croft, N. Jisrawi, Z. Zhong, R. Holtz, M. Shepard, M. Lakshmipathy, K. Sadananda, J. Skaritka, T. Tsakalakos, Eng. Mater. Technol. 130 (2008) 021005.
[12] M. Croft, V. Shukla, E.K. Akdoğan, N. Jisrawi, Z. Zhong, R. Sadangi, A. Ignatov, L. Balarinni, K. Horvath, T. Tsakalakos, J. Appl. Phys. 105 (2009) 093505.
[13] A. Steuwer, J.R. Santisteban, M. Turski, P.J. Withers, T. Buslaps, Nucl. Instrum. Methods Phys. Res. Sec. B 238 (2005) 200.
[14] N. Scarlett, I. Madsen, J. Evans, A. Coelho, K. McGregor, M. Rowles, M. Lanyon, A. Urban, J. Appl. Cryst. 42 (2009) 502.
[15] C.J.J. Van Loon, D.J.W. Ijdo, Acta Crystallogr. B31 (1975) 770.
[16] K. Adendorff, M. Thackeray, J. Electrochem. Soc. 135 (9) (1988) 2121.
[17] K. Suzuki, J. Phys. Soc. Jpn. 16 (1961) 67.
[18] J. Gomez Sal, F. Rodriguez, M. Moreno, J. Tholence, Phys. Rev. B37 (1988) 454.
[19] M. De Lucas, F. Rodriguez, M. Moreno, Phys. Stat. Solidi B184 (1994) 247.